University of Groningen

X-ray Nanospectroscopy Reveals Binary Defect Populations in Sub-micrometric ZnO Crystallites

Hageraats, Selwin; Keune, Katrien; Stankic, Slavica; Stanescu, Stefan; Tromp, Moniek; Thoury, Mathieu

IMPORTANT NOTE: You are advised to consult the publisher's version (publisher's PDF) if you wish to cite from it. Please check the document version below.

Document Version
Publisher's PDF, also known as Version of record

Link to publication in University of Groningen/UMCG research database

Article

X-ray Nanospectroscopy Reveals Binary Defect Populations in Sub-micrometric ZnO Crystallites

Selwin Hageraats,* Katrien Keune, Slavica Stankic, Stefan Stanescu, Moniek Tromp, and Mathieu Thoury

Read Online

ACCESS | Metrics & More | Article Recommendations | Supporting Information

ABSTRACT: Besides its many applications in electronics, photonics, and catalysis, ZnO has also been extensively used as the pigment zinc white ever since its introduction in the first half of the 19th century. It is shown here that zinc whites (ZnO formed through zinc vapor oxidation) form a chemically binary system, with each of the sub-micrometric crystallites belonging to either of two distinct classes. The observation of the two classes is done based on X-ray absorption nanospectroscopy and was determined to be caused by differences in the populations of anisotropic crystal defects. A theoretical assessment of the vapor oxidation synthesis method is formulated that predicts that the binary distinction in crystal defect populations is caused by local variations in synthesis parameters. As the crystal defect population in ZnO has been shown to be related to its catalytic properties, these results provide fundamental insights on the link between the intrinsic properties of zinc white and its degradation issues in oil paint.
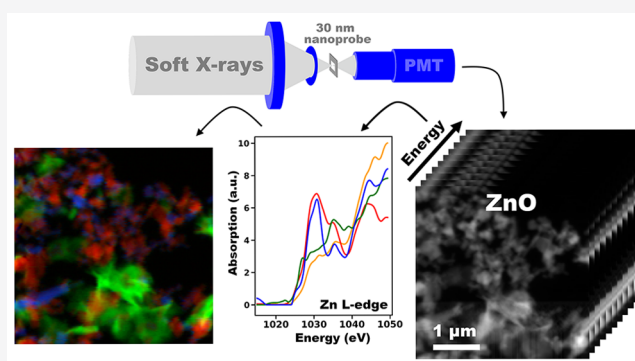
INTRODUCTION

Zinc white has been a popular choice of white pigment since it was commercially introduced as a less toxic alternative to lead white in the first half of the 19th century.[1] Its use in oil paints is widespread among well-known artists such as Vincent van Gogh, Paul Cézanne, and Piet Mondrian. However, it has been known, or at least strongly suspected, since the early 20th century that zinc white reacts with the fatty acids released through hydrolysis of the drying oil binding medium to form zinc soaps. Although experimental evidence of soap formation was already reported in 1941 by Jacobsen and Gardner,[2] extensive research into this phenomenon did not start until the early 2000s. Current studies on metal soaps in oil paint cover a broad range of aspects, including their description in historical works of art,[3,4] formation and migration properties,[5,6] and methods of characterization.[7,8] The extent of zinc white-related degradation found in different paintings varies widely: whereas Rogala et al.[3] report on some severe cases of paint delamination, most paintings that contain zinc white are in much better condition. A recent study into the zinc soap formation in a 1917 painting by Piet Mondrian even shows variability in the extent of degradation between adjacent paint layers with highly similar composition.[9] In general, two groups of factors are thought to have an effect on the rate of degradation of zinc white: environmental factors (e.g., humidity, temperature, light, cleaning agents, and air pollutants)[10,11] and compositional factors (e.g., stratigraphy, metal carboxylate driers, and other pigments).[11−13]

Despite the plethora of studies that explore the effect of environmental and compositional factors, the effects of the intrinsic properties of zinc white on its own degradation have been discussed to a much lesser degree. The main argument for involving the intrinsic properties of zinc white in the study of oil paint degradation is the widely studied catalytic activity of ZnO, which is generally thought to be caused by intrinsic surface defects. This link has been established through both theoretical and experimental studies.[14−18] In this context, it is of specific interest to note the high catalytic activity of ZnO for the transesterification of vegetable oils with methanol.[17,18] This reaction is highly similar to the hydrolysis of vegetable oil, the only difference being that instead of water (H−OH), methanol (CH₃−OH) substitutes the glycerol backbone. As discussed earlier, it is precisely this hydrolysis of vegetable oil that causes the formation of problematic zinc soaps in zinc white oil paints. Although it remains unclear how the catalytic activity of ZnO in transesterification reactions under extreme industrial
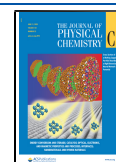
conditions translates to its catalytic activity in the hydrolysis of oil paints, these studies do support the potential interest of studying the intrinsic defect chemistry of zinc whites.

By making use of the photoluminescence emission associated with certain crystal defects, it has been verified that there is variation among the defect chemistry of different batches of zinc white.[19−23] Considering the history of zinc white production, the observation of some variability is actually in line with expectation. It is, for instance, well-known that the production of zinc white has historically occurred by means of two distinct processes: the French (or indirect) process, in which metallic zinc is vaporized and subsequently oxidized, and the American (or direct) process, in which zinc ore is used instead of metallic zinc.[1] Further variability in the characteristics of zinc white is expected as a result of variations in synthesis conditions and design of the production furnaces.

In the work of Bertrand et al.,[19] it was shown that, based on photoluminescence characteristics, not only is it possible to discriminate between different batches of zinc white, but also between the individual ZnO crystallites within a batch. In order to fully understand how the intrinsic defect populations in zinc white affect its chemical activity in an oil paint, it is therefore of high interest to study its defect chemistry on the scale of the individual sub-micrometric (∼200 nm) zinc white crystallites. Since the catalytic activity of ZnO takes place on its surface, it is also highly preferable to be able to resolve the crystallite size and morphology.

The aim of this study was therefore to develop a methodology that is able to simultaneously characterize the defect chemistry and morphology of the sub-micrometric ZnO crystallites that constitute the zinc white pigment. The approach taken here is based on scanning transmission X-ray microscopy in the soft X-ray regime. In the energy range, a Fresnel zone plate (FZP) enables lateral resolutions of less than 10 nm.[24] Recording the X-ray absorption near-edge structure (XANES) at the Zn L-edge (∼1030 eV) is anticipated to provide information about the average coordination environment of individual particles, which is thought to be affected by (intrinsic) crystal defect populations.[25−28] Besides clear implications for the study and conservation of oil paint, the material properties reported here are also critical for the extensively studied applications of ZnO in catalysis, photonics, and electronics.

■ METHODS

Sample Preparation. Samples of six different batches of zinc white were analyzed. Five of these were reportedly produced using the indirect (French) vapor oxidation process, and one was produced using the direct (American) vapor oxidation process. The direct process sample, as well as two of the indirect process samples, were acquired from historical collections, whereas the three remaining indirect process samples were obtained from modern pigment manufacturers. Reference codes were used that list the production process (FR, AM), whether the sample was obtained from a historical collection or from a modern manufacturer (Hist, Mod), and an indexing number. In addition, a high-purity, lab-synthesized ZnO was studied as a reference.

The high-purity, lab-synthesized ZnO was synthesized by using the vapor oxidation process, combusting Zn-foil (high purity 99.99%, 0.125 mm thickness, Advent Research Materials Ltd.) in a glovebox made of stainless steel and designed to be put under vacuum. After three alternating cycles (outgassing

and purging with Ar), a mixture of Ar/O₂ = 80/20 (Air Liquide, purity Ar > 99.99% and O₂ > 99.995%) was introduced into the glovebox up to $P = 1$ bar, and the pure ZnO powder was collected in the inert atmosphere on a glass plate. X-ray photoelectron spectroscopy (XPS) analysis of the lab-synthesized batch showed no detectable impurities.

All seven ZnO samples were prepared for scanning transmission X-ray microscopy (STXM) analysis by suspending ∼300 μg of powder in ∼1 mL of isopropanol, sonicating the suspension for several minutes, and then casting a ∼5 μL droplet of the suspension onto a 100 nm thick silicon nitride window heated to 100 °C. Within several seconds, all isopropanol evaporated, leaving small amounts of powder dispersed over the surface of the silicon nitride window.

STXM Analysis. STXM experiments were conducted at the HERMES soft X-ray beamline of the SOLEIL synchrotron (Saint-Aubin, France). During these experiments, the microscope (Research Instruments GmbH) was equipped with a 30 nm outer ring width FZP lens and a 50 μm order sorting aperture to focus the monochromatized beam down to a size of approximately 40 nm. Experiments were conducted in a vacuum chamber pumped to 10^{-3} mbar. Silicon nitride windows supporting the various zinc white samples were fixed to an XYZ scanning stage, Z being the direction colinear with the X-ray beam propagation and used to bring the sample onto the FZP focal plane. A STXM image is obtained in raster mode as a function of the XY position, each pixel intensity following the Beer−Lambert absorption law. Transmitted photons are measured using a photomultiplier tube (PMT), and the X-ray energy is tuned to yield hyperspectral images (energy stacks) of clusters of 20−200 mostly unstacked ZnO crystallites. The typical X-ray energy range used to measure the Zn L-edge was 1015−1050 eV, with 0.15−0.3 eV spectral resolution. All drop-cast ZnO samples present thicknesses permitting sufficient signal for low-noise data to be recorded with a 3 ms per pixel dwell time. The single-energy images making up the energy stacks were recorded by continuously scanning the XY translation stage (constant velocity mode), recording the integrated signal every 50−70 nm over a ∼5 × 5 μm² scanning range. For each sample, additional images were recorded at 20−30 nm step size at 1010 and 1035 eV (before and after the Zn L-edge).

STXM Data Processing. The STXM energy stacks were preprocessed and then analyzed using the simplex volume maximization (SiVM) endmember selection algorithm.[29] Endmembers obtained through SiVM are spectra that are mathematically determined to be the set of basis spectra that produce linear combination fits of the remaining data with the smallest sum of squared errors. Due to this property, endmember spectra are generally considered to represent the *pure* compounds or phases. In the absence of other compounds or crystalline phases, endmember spectra selected from XANES analyses of pure zinc whites are expected to reflect heterogeneities in average coordination chemistry, with an anticipated link to intrinsic defect populations. An SiVM implementation in Python was based on the DataHandlerP software and used to produce spectral endmembers that are passed as input factors for non-negative least squares (NNLS) fitting. A more detailed description of this approach is provided in Supporting Information.

X-ray Diffraction. X-ray diffractograms (XRD) of the zinc white samples were recorded using a Rigaku MiniFlex II desktop diffractometer with a Cu Kα radiation source. Samples
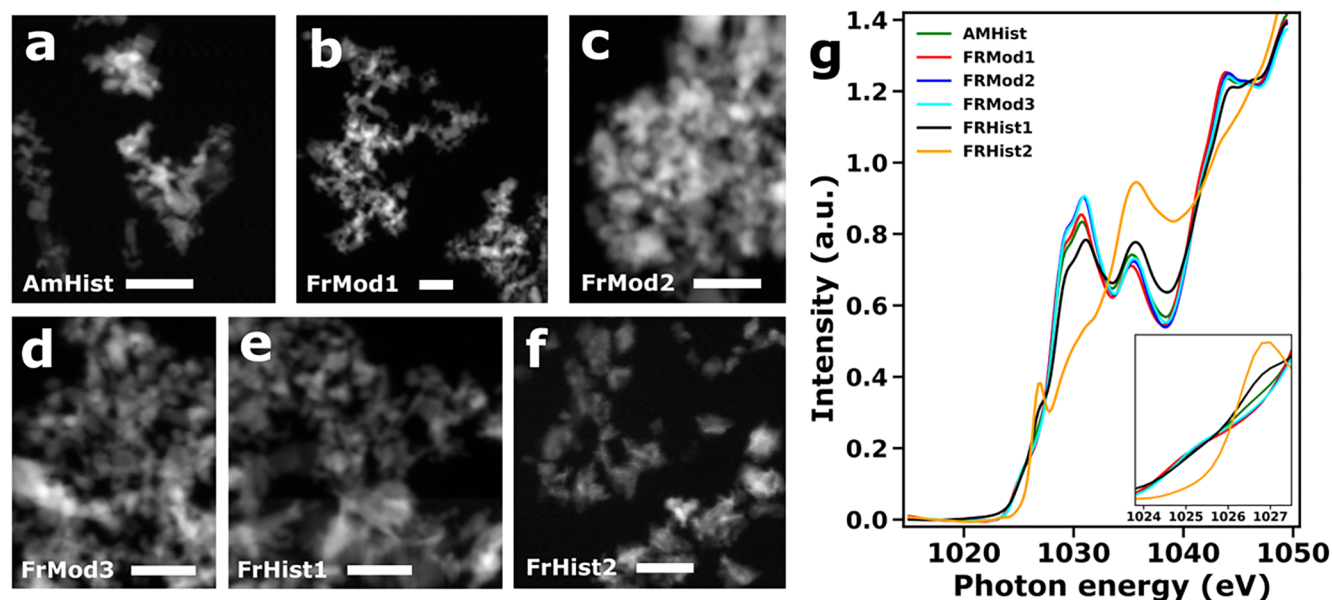
Figure 1. OD STXM images of the six studied zinc whites, each recorded with a photon energy of 1035 eV (a−f) and the corresponding average Zn L-edge XANES spectra (g). The inset in panel g shows a magnification of the pre-edge absorption features. All scale bars have a length of 1 μm.
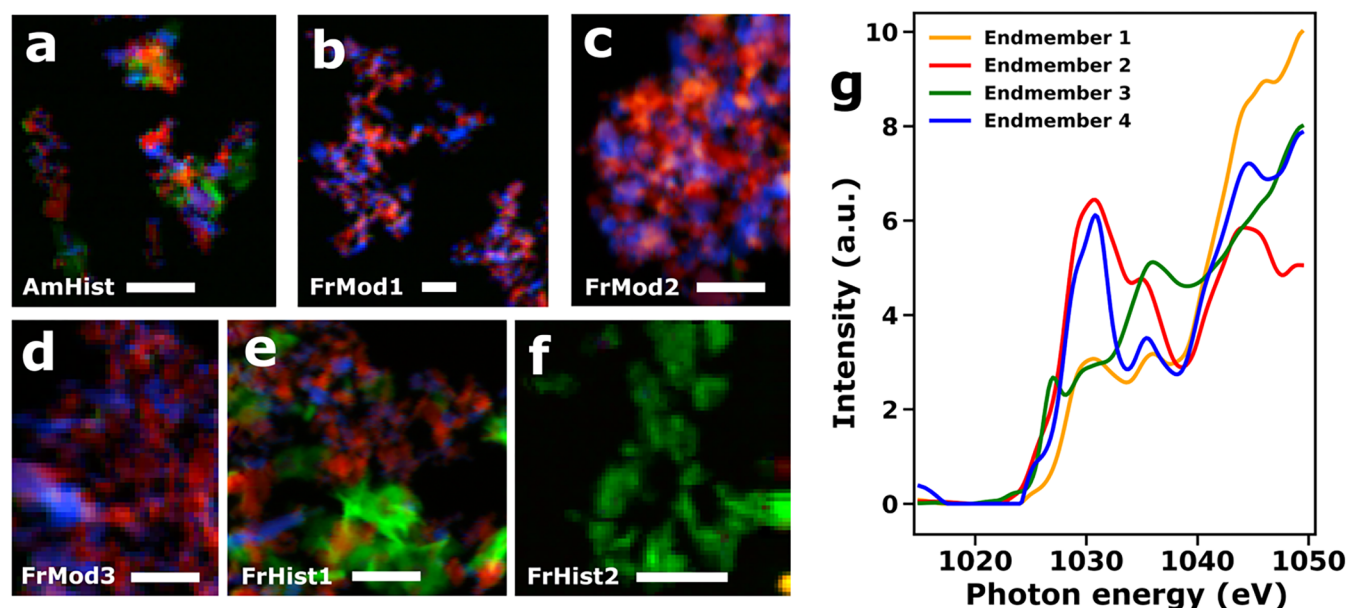
Figure 2. False color images based on NNLS weight matrices for spectral endmembers 2−4 (a−f) and a plot of endmembers 1−4 (g), with the colors of endmembers 2−4 corresponding to their mappings in panels a−f. All scale bars have a length of 1 μm.

were analyzed in a $2\theta = 10-75°$ angular range at a 5°/min scan velocity and 0.05° resolution.

RESULTS

High-resolution optical density (OD) STXM images were recorded on each sample at photon energies of 1035 and 1010 eV (right after and right before Zn L-edge) to determine particle size and morphology, reveal possible contaminations, and verify whether the sample preparation yielded sufficiently dense particle dispersions without excessive stacking. Multi-energy stacks were recorded at lower lateral resolutions to retrieve full Zn L-edge XANES spectra on each of the particles in view. The images recorded at 1035 eV are shown in Figure 1a−f. Particle size and morphology differ from sample to sample, but generally speaking the batches consist of nodular or rod-like grains with sizes of about 200 nm, in line with what is typically reported for zinc white.[1] Images are dominated by particles exhibiting a uniformly low OD, with only a few highly absorbing clusters. Subtracting images recorded at 1010 eV (before Zn L-edge) from those recorded at 1035 eV (at Zn L-edge) revealed a large increase in OD for all observed particles. These observations suggest that the drop-casting sample preparation method (see Methods) yields well-dispersed particles, all consisting of zinc compounds. Figure 1g shows the average XANES spectrum per sample, calculated from the corresponding multienergy stack. The inset on the bottom right shows the 1024−1027.5 eV spectral region in more detail. All samples show comparable absorption spectra, with the

exception of samples FrHist1 and FrHist2. FrHist1 exhibits a significant pre-edge at 1027 eV and a nearly 1:1 ratio of the 1031 and 1036 eV absorption features, whereas FrHist2 exhibits an even stronger absorption at 1027 eV and a radically different spectrum in the 1029−1040 eV energy range. Still, it is evident that at least four batches of zinc white cannot readily be discriminated solely on the basis of average X-ray absorption properties.

To determine how the differences and similarities between the different batches of zinc white present themselves on the nanoscale, the multienergy stacks were factorized into four endmember spectra using SiVM and subsequently modeled using non-negative least-squares (NNLS). Figure 2a−f shows false color images with the NNLS weight matrices of endmembers 2, 3, and 4 used as the red, green, and blue channel, respectively. The specific choice for endmembers 2−4 was made based on the very low covariance between their three weight matrices, indicating that each maps a different, spatially uncorrelated chemical species. Plots of spectral endmembers 1−4 are shown in Figure 2g. Each set of four weight matrices was normalized to a common maximum, so as to maintain proportionality and enable qualitative comparison among samples. In Figure 2a−f, a clear variation in the X-ray absorbing properties among different ZnO particles can be observed. This variation is most apparent in the three FrMod samples (Figure 2b−d), where particles can be binarily classified as having properties similar to either endmember 2 (red) or endmember 4 (blue). This distinction can also be observed in samples FrHist1 and AmHist, although here, besides the red and blue grains, a considerable number of particles appear with a distinct green color, indicating X-ray absorption similar to endmember 3 (Figure 2a,e). Sample FrHist2 even seems to fully consist of grains with a green signature (Figure 2f).

X-ray diffractograms of the six zinc white samples are shown in Figure 3. The diffractograms suggest that the major phase in
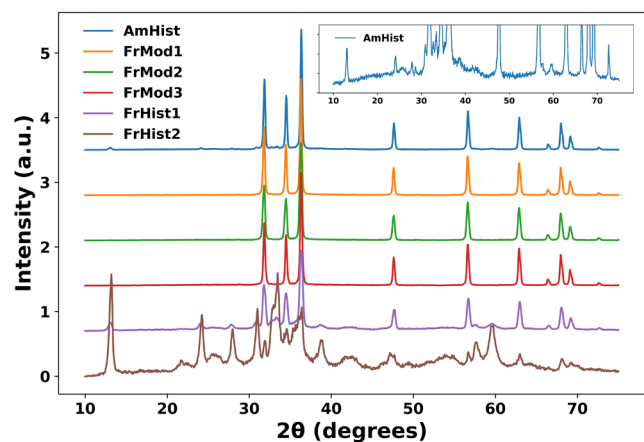
Figure 3. XRD diffractograms of the six zinc white samples. The inset in the upper right of the figure shows an enlargement of the AmHist diffractogram in which the minor phase can clearly be distinguished.

five out of six samples is wurtzite ZnO. The only exception here is sample FrHist2, which exhibits an entirely different diffractogram. This particular compound can also be observed as a minor phase in samples AmHist (inset) and FrHist1. These particular diffractograms were found to match with hydrozincite $(Zn_5(OH)_6(CO_3)_2)$: a basic zinc carbonate.[30]

This observation allows us to unambiguously identify the grains with the green signature in Figures 2a,e,f as hydrozincite.

DISCUSSION

The consistent appearance of all ZnO particles in the false color images as either red, blue, or green, but rarely a mix of colors, raises questions about the chemical origin of the observed contrast and its relation to the production process. Since this phenomenon has not been previously described in the literature, the following discussion aims to propose an interpretation based on previously established knowledge of the origin of Zn L-edge XANES absorption features and their symmetries and the theoretical literature on crystal defects in ZnO.

Identification of Absorption Features. The intensities of XANES absorption features are directly related to the unoccupied density of states (DOS). In the case of Zn L-edge XANES, in accord with the dipole-transition selection rule, the unoccupied DOS being probed is that of the Zn 4s and Zn 4d derived states, with the Zn 2p orbitals as the lower energy levels of the transitions. Large (∼15 eV) spin−orbit coupling effects of the $2p^5$ core hole cause the spectrum to be split into an L_3- and L_2-edge, corresponding to $J = 3/2$ and $J = 1/2$ final states, respectively. In this discussion, we will focus on the Zn L_3-edge, which spans roughly from 1025 to 1040 eV.

From the previously reported low anisotropic response of the small absorption feature at 1025 eV (most clearly visible in Figure 1g), it was concluded that this feature can be attributed to a transition to mostly isotropic Zn 4s derived states.[26] The same study found a stronger anisotropic response of the features between 1029 and 1037 eV, supporting their attribution to transitions to directional Zn 4d derived states. Theoretical orbital-specific Zn L-edge XANES obtained through the FEFF software supports the assignment of the 1025 eV absorption feature but also assigns the transition of 1029 eV to a Zn 4s derived state.[31] The anisotropic nature of this absorption feature, as demonstrated by Chiou et al.,[26] could then simply be interpreted as being due to strong overlap with the broad tails of the nearby transitions to Zn 4d derived states. From the splitting in d-orbital energy levels predicted by crystal field theory for tetrahedrally coordinated compounds, at least two main absorption features are expected, corresponding to transitions to the e_g and t_{2g} Zn 4d orbital groups. Electron−electron repulsion and spin−orbit coupling further split up the possible transitions into a more complex spectrum,[32] explaining the observation of at least three visually discernible absorption features: 1031, 1032.5 (shoulder), and 1036 eV. Finally, the sharp 1027 eV absorption feature that is only visible in endmember 3 can be ascribed to hydrozincite. It most likely corresponds to a transition to Zn 4s derived states and is indicative of octahedral Zn coordination.[33,34]

Assessment of STXM Contrast in Terms of Lattice Defects. In order to now fully interpret the contrast shown in Figure 2, average normalized Zn L-edge XANES spectra of the red, green, and blue ZnO particles are shown in Figure 4. These average spectra represent most accurately what the X-ray absorption behavior is of particles that score high on either endmember 2, 3, or 4 (red, green, and blue, respectively). Interpretation was not done directly from the spectral features of the endmembers themselves, because these endmembers are the *purest* representation of each phase, and the typical particles with red, green, and blue signatures may in fact exist as mixtures of the pure phases with certain preferential mixing
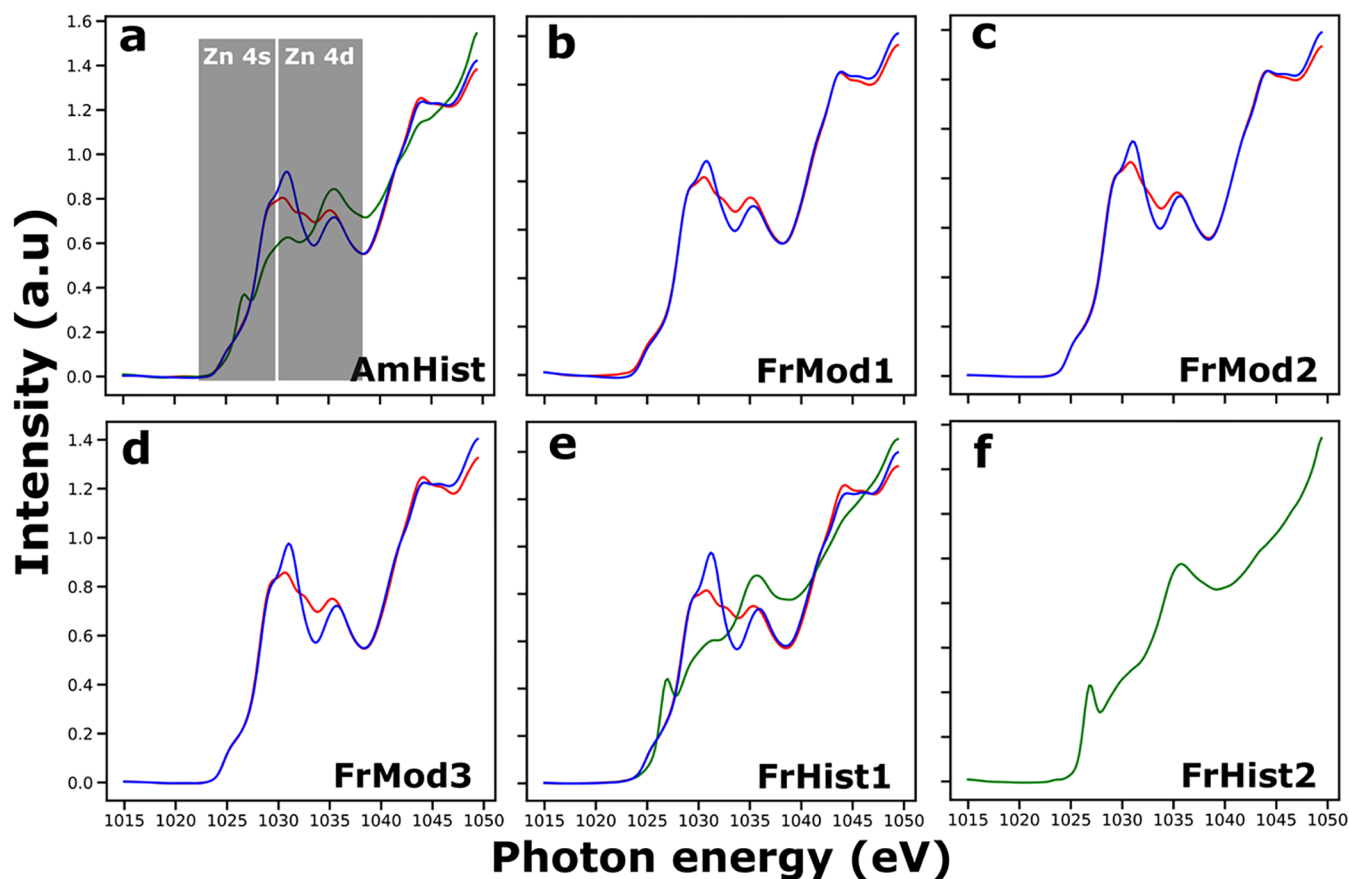
Figure 4. Average normalized Zn L-edge spectra of the ZnO crystallites determined from the data shown in Figure 2 to have a predominantly red, green, or blue signature. The colors of the spectra correspond to the color coding used in Figure 2. For the data sets where predominantly green ZnO particles are absent, a spectrum is not shown.
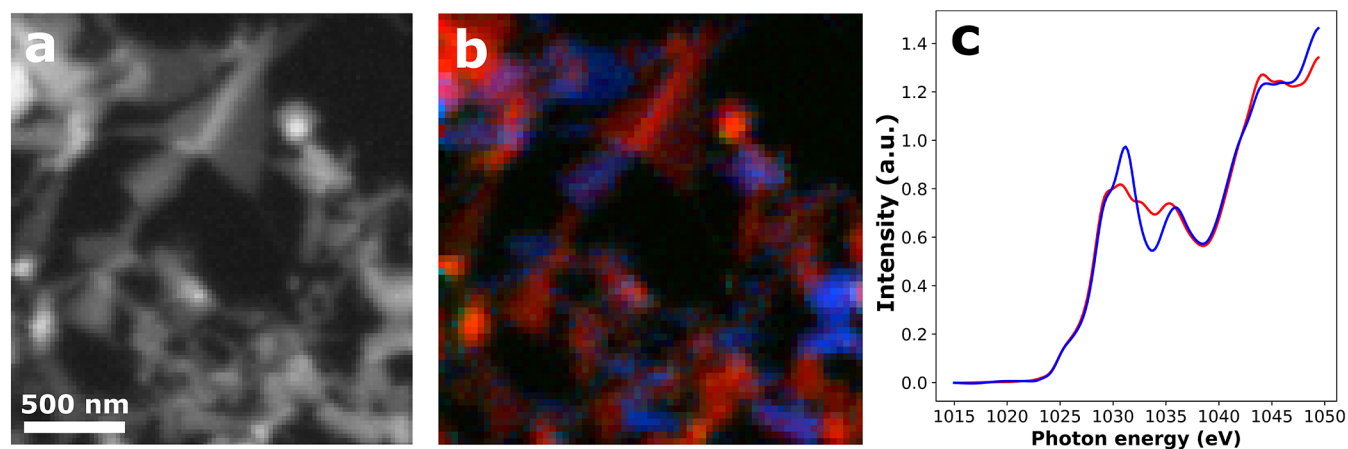
Figure 5. STXM analysis of the ultrapure lab-synthesized ZnO sample. High-resolution transmission image (a), SiVM-NNLS false color image (b), and the average normalized Zn L-edge spectra of the ZnO particles determined to have a predominantly red and blue contribution.

ratios. As the particles with a green signature have already been identified as hydrozincite, the following discussion will focus on the as of yet unexplained blue–red contrast.

For all samples, it is clear that ZnO particles with a red and a blue signature are distinguished by deviations in the absorption between 1031 and 1036 eV. To be precise, particles with a blue signature can be distinguished from those with a red signature by a more intense absorption feature at 1031 eV and a less pronounced shoulder at 1032.5 eV. On the other hand,

features below 1030 eV, related to transitions to Zn 4s derived states, seem unaffected. Considering the peak interpretation discussed earlier, this means that red and blue fractions have a highly similar density of unoccupied Zn 4s derived states but exhibit differences in the densities of certain symmetrically distinct unoccupied Zn 4d derived states.

To exclude impurities as the leading cause for this distinction in electronic properties, Figure 5 shows the false color image of an ultrapure ZnO sample. The observation that

a clear binary distinction is maintained between a red and a blue fraction strongly suggests that impurities, with the exception of hydrogen, cannot be related to the existence of two separate ZnO fractions. Likewise, the fact that the two fractions have an identical density of Zn 4s derived states (i.e., the states lying in the lowest part of the conduction band) suggests that the electron donating properties of some defects (e.g., H_i, Zn_i, ZnO)[35−37] do not play a direct role either. Rather, the distinction is expected to be related to distortions in the crystal lattice with a strongly anisotropic character. This can be inferred from the previously made observation that the differences between ZnO particles with red and blue signatures only show up in Zn L-edge XANES features that are themselves anisotropic (i.e., the Zn 2p to Zn 4d transitions). This excludes lattice distortion by oxygen vacancies (V_O), zinc vacancies (V_{Zn}), and zinc interstitials (Zn_i) as the direct source of this distinction, as these point defects have spherical (a_1) symmetry in all charge states.[38−40] Oxygen interstitials (O_i), on the other hand, have been shown both theoretically and experimentally to exist in a number of configurations, all of which are electronically anisotropic.[39−42] Zinc antisites (zinc atom on oxygen lattice site, denoted Zn_O) are another type of intrinsic crystal defect for which DFT calculations suggest that the energetically most favorable configuration is anisotropic.[42] A similar effect was found for oxygen antisites (oxygen atom on zinc lattice site, denoted O_{Zn}), for which an energetically favorable displacement of over 0.7 Å along the [0001] direction is predicted.[42]

Besides electronically anisotropic point defects, complexes of two or more intrinsic point defects may also induce anisotropic lattice distortions, as they can be assumed to exhibit a preferential configuration. Little is known about such complexes; the reason for which may be either the unfavorable energetics of bringing point defects close together or the relatively low energy barriers for defect migration.[37,43] Only the V_O−Zn_i complex has been described in more detail and has been associated with the intrinsic n-type character of ZnO.[43,44] Calculations show a lower formation energy of the V_O−Zn_i complex than of the two separate point defects and an increased migration energy barrier for Zn_i when brought within 3.6 Å of V_O.[43] Especially high-temperature, oxygen-deficient synthesis conditions may favor the formation of such defect complexes.

From this comprehensive assessment of the symmetries of the most commonly reported crystal defects in ZnO, one must conclude that, based on the interpretation of the XANES absorption features alone, no specific species can be appointed as the cause for the observed binary distinction between ZnO particles. Rather, it can be narrowed down to those that have an anisotropic electronic structure: O_i, O_{Zn}, Zn_O, and the V_O−Zn_i complex. The question that remains now is how these anisotropic defects can lead to the stark red−blue binary distinction between particles that is shown in Figures 2 and 3?

The Relation between STXM Contrast and ZnO Production. In order to postulate a viable answer to this question, it is worth considering that different defects have different formation energies that depend on the Fermi level and on the chemical potential of Zn and O during synthesis.[37,39,40,42] Several studies show that the defect formation energy E^f typically depends on the Fermi level, E_F, with a slope $\left|\dfrac{\partial E^f}{\partial E_F}\right|$ on the order of 2.[37,39,40,42] The slope $\left|\dfrac{\partial E^f}{\partial \mu}\right|$ of E^f relative to the chemical potentials μ of Zn and O is a bit

harder to express, but between their theoretical lower and upper bounds, values for E^f have been calculated to typically lie 3−4 eV apart.[37,39,40,42] Under the assumption of thermodynamic equilibrium, the concentration of defects is a function of E^f following a Boltzmann distribution.[45] Due to this exponential relationship, relatively small changes in the Fermi level or chemical potentials can have a large effect on the crystal defect populations of a ZnO crystallite. This can be illustrated by calculating the ratio $R_{i,j}$ between concentrations of the same type of crystal defect for crystallites i and j synthesized under different conditions:

$$R_{i,j} = \frac{e^{-E_i^f/(k_B T)}}{e^{-E_j^f/(k_B T)}} = e^{\Delta E^f/(k_B T)}$$

Here, k_B is the Boltzmann constant, T is the temperature, and ΔE^f is the difference in formation energy $E_j^f - E_i^f$, resulting from the difference in synthesis conditions. For a typical synthesis temperature of 1200 K, a ratio $R_{i,j}$ of 10 is found for a ΔE^f of just 0.24 eV. Given the previously mentioned estimates of $\left|\dfrac{\partial E^f}{\partial E_F}\right|$ and $\left|\dfrac{\partial E^f}{\partial \mu}\right|$, such an increase could typically be realized by as little as a 0.12 eV change in E_F or a 6−8% shift in μ_{Zn} or μ_O. Moreover, the relations $E^f(E_F, \mu_{Zn}, \mu_O)$ for different crystal defects exhibit a large variation, with positive, negative, and (partially) negligible slopes, meaning that the ratio between concentrations of *different* defects can differ as much as 2 orders of magnitude for the listed shifts in E_F, μ_{Zn}, and μ_O. Although the Boltzmann distribution predicts no upper limit to the concentrations of crystal defects, it is expected that a saturation effect dominates toward very high defect concentrations. Considering the trivial lower limit in defect concentrations of 0, one may then expect that even small differences in E_F, μ_{Zn}, and μ_O during synthesis yield ZnO crystallites of which the vast majority has either of two distinct defect populations. As there are therefore also two distinct populations of low-symmetry defects, the ZnO crystallites can be predicted to exhibit a mostly binary distinction in the Zn L-edge XANES. Alternatively, one may expect a saturation effect in the extent to which large populations of low-symmetry crystal defects map onto the unoccupied DOS of the Zn 4d derived states. This yields a similar result; with two distinct DOS of Zn 4d derived states producing a binary distinction in the Zn L-edge XANES. Both hypotheses predict S-shaped curves for the defect concentration as a function of E_F, μ_{Zn} and μ_O, of which the position of the inflection point depends on the type of defect.

Given the typical vapor oxidation fabrication processes of zinc white, in which either metallic zinc or zinc ore is vaporized and subsequently oxidized,[1] it is to be expected that the chemical potentials of Zn and O vary as a function of the distance from the zinc source. As the zinc vapor moves farther away from the source, the local partial pressure of Zn and therefore μ_{Zn} decreases. It is therefore expected that somewhere along the way from the zinc source toward the end of the oxidation chamber, the slowly changing formation energies will cause a tipping point (S-curve inflection point) for the concentrations of certain crystal defects. Before and after this tipping point, two distinct types of ZnO will precipitate, together forming a batch with a binary chemical distinction. As different defects can be predicted to have different tipping points, there is likely only one defect or defect complex responsible for this binary behavior.

From ZnO to Hydrozincite. Having determined the chemical nature and origin of the grains with a blue and red signature, this still leaves the hydrozincite phase largely undiscussed. Although the finding of (basic) zinc carbonates in samples of zinc white is not entirely new,[1,10,46] their nomenclature is ambiguous and often inconsistent.[47] Here, for the first time, the dominant carbonate phase could be identified explicitly as hydrozincite. As hydrozincite can be synthesized from ZnO through exposure to CO_2/H_2O atmospheres,[48] it is hypothesized that this phase is in fact a degradation product of zinc white, resulting from prolonged atmospheric exposure during its storage. This is mostly in line with the age of the analyzed zinc white batches and the hydrozincite fraction found using XRD. Samples FrHist1 and FrHist2 come from historical collections and exhibit either complete conversion or the presence of a significant minor hydrozincite phase, the AmHist sample comes from a much younger museum collection and also has relatively low concentration of hydrozincite, whereas the three modern pigments (FrMod1−3) contain no observed fraction of hydrozincite.

Besides identifying for the first time the dominant carbonate degradation phase of zinc white, STXM analysis of samples FrHist1, FrHist2, and AmHist also directly shows its nanometric spatial distribution. Contrary to what would be expected from a degradation product formed under the influence of atmospheric compounds, the hydrozincite phase is not observed as partially converted ZnO crystallites but rather exists as separate crystallites without a well-defined dominant morphology. From this observation, it can be hypothesized that either partial conversion does occur but the two phases are mechanically insufficiently stable to remain attached during the STXM sample preparation or certain ZnO crystallites are more reactive toward CO_2 and water than others, causing some to be completely transformed to hydrozincite while others remain unaffected. Whether or not the second hypothesis is reflected in the STXM data can be tested by considering the false color image of sample FrHist1 shown in Figure 2. This is the only sample with a hydrozincite concentration that allows us to see an effect on the binary populations of crystallites with blue and red signatures. Although the number of particles of sample FrHist1 captured in the field of view is insufficient for sound statistical analysis, it appears to be the case that the fraction of ZnO crystallites with a blue signature is lower than in samples FrMod1 and FrMod2. This does suggest that a difference exists in the tendency of the two different types of ZnO crystallites to react with CO_2 and water and form hydrozincite. This tendency would be in line with an earlier study in which it was shown that ZnO from different batches of zinc white exhibit different reactivity toward atmospheric sulfur compounds.[11]

Comparison of STXM Contrast to PL Contrast. At this point, it is worth recalling the comments made in the Introduction with regards to the differences in photoluminescence behavior among different batches of zinc white and between the individual ZnO crystallites within a batch.[19] As there is broad consensus that the relative intensities of these emission bands are related to intrinsic defect populations, this section aims to explore briefly the parallels with the binary contrast in X-ray absorption behavior that is described in this article. First, it must be noted that the two most widely described trap state emissions (violet and green, mapped out in Bertrand et al.[19]) are typically ascribed to Zn_i and V_O,

respectively,[23] which due to their a_1 symmetry are not thought to have a direct relationship to the binary X-ray absorption contrast.[38−40] Moreover, contrary to X-ray absorption, photoluminescence emission exhibits an extraordinarily large dynamic range, with 50-fold differences in integrated photoluminescence intensity demonstrated between batches.[19] This variability in emission intensity is thought to be tightly related to the de-excitation pathways related to band gap emission and various nonradiative processes. All such de-excitation pathways are affected by the overall crystallinity and are in direct competition with each other. Thus, the intensity of one emission band is to some extent related to the intensities of all others. As such competition is not expected to significantly influence the relative intensities of X-ray absorption features, quantitative relationships between intrinsic defect concentrations and spectral feature intensities are thought to be completely different for photoluminescence and XANES.

Despite these undeniable dissimilarities, there may be two ways in which photoluminescence and X-ray absorption contrast are related. One way would be if the binary distinction in X-ray absorption behavior is caused by a crystal defect that has a PL-active trap state. The V_O-Zn_i complex itself may act as a PL-active trap state, although no consensus exists about its exact nature and PL emission wavelength. Some calculations propose that V_O-Zn_i could act as a shallow donor, explaining observations of n-type conductivity in ZnO,[43,44] whereas another calculation predicts the V_O-Zn_i complex to be a deep donor.[50] The electronically anisotropic O_i defect has been associated with yellow emission (~2 eV), but this band is was only demonstrated under very specific conditions that strongly favor the formation of O_i.[23,49]

The second way considers possible statistical correlations between the defect that causes the binary distinction in X-ray absorption behavior and the population of PL-active defects. For instance, even if the V_O-Zn_i complex itself is not PL-active, its concentration is still likely to be tightly correlated to the concentrations of the separate, PL-active V_O and Zn_i point defects. A general statistical relationship between electronically anisotropic and PL-active defects can also be hypothesized based on the previously discussed relationship between chemical potentials μ_{Zn} and μ_O, defect formation energies, and defect concentrations. In essence, the two classes of ZnO crystallites, as distinguished based on Zn L-edge XANES, reflect the local chemical potentials during synthesis. These local chemical potentials also affect the populations of PL-active defects, but their concentration tipping points do not necessarily coincide with the tipping point that causes the binary distinction in X-ray absorption. The existence of such tipping points predict that ZnO crystallites can also be subdivided into certain classes according to photoluminescence behavior, as was also experimentally shown by Bertrand et al.[19] As both classifications depend on the same variables (i.e., μ_{Zn} and μ_0), class membership in X-ray absorption will be a predictor for class membership in photoluminescence behavior. The extent to which one membership can predict the other then reflects how close the tipping points are on the chemical potential axis.

Implications for Oil Paint Degradation. As was set forth in the Introduction of this article, the prime motivation of this study was the hypothesis that intrinsic crystal defects in ZnO may act as catalytically active sites in the hydrolysis of oil binding media. The results shown in this article reveal that zinc whites form a distinctly binary chemical system. This chemical

contrast could be ascribed to differences in the populations of electronically anisotropic intrinsic crystal defects. These differences are postulated to be caused by spatial variation of the chemical synthesis parameters. With respect to catalytic activity, the electronically isotropic oxygen vacancies are typically identified as the active sites in ZnO.[14−16] As was discussed in the previous section of this article, these defects may not directly affect the X-ray absorption behavior, but they are still expected to be distributed over the ZnO crystallites in a comparable binary manner. The STXM−XANES method discussed here does not seem to be able to observe this catalytically relevant binary system, but due to a shared thermodynamic origin, it is expected to be tightly related to populations in the observable binary system.

The question now is whether STXM−XANES could indeed allow characterization of the reactivity of a pigment as a whole. The answer relies primarily on whether ZnO does indeed acts as catalyst in the hydrolysis of oil binders and whether oxygen vacancies indeed act as the catalytically active sites. Although previous studies do point in this direction,[14−18] further investigations will be necessary to establish this relationship. Under the assumption that these hypotheses are accurate, it is possible to postulate a metric that allows characterization of a batch of ZnO by means of STXM−XANES in terms of its reactivity in oil binders. This metric, A_C, measures the oxygen vacancy-rich surface area per unit weight of a zinc white sample. The possible accuracy of this measure heavily relies on the extent to which the STXM−XANES signature of a crystallite predicts its signature in the unobservable catalytically relevant binary system. Under the assumption that the signature in the observable binary system perfectly predicts the signature in the unobservable binary system, a STXM−XANES map covering a large number (i.e., hundreds) of ZnO crystallites would provide sufficient data to calculate A_C. When this assumption does not hold, the accuracy of the metric A_C will be lower but may still prove useful as a means to rank zinc whites in terms of catalytic activity.

CONCLUSION

Intrinsic crystal defects in ZnO are thought to be catalytically active in the degradation of the drying oil binding medium of oil paints and could thereby foster the subsequent formation of zinc soaps. The ability to characterize ZnO in terms of crystal defects is therefore deemed vital to obtain a comprehensive understanding of the problematic nature of the zinc white pigment. Scanning transmission X-ray microscopy (STXM) has been shown for the first time to allow clear chemical differentiation between individual ZnO crystallites produced using the vapor oxidation synthesis method. Through a factorization by means of simplex volume maximization (SiVM) and subsequent fitting using non-negative least-squares (NNLS), it was demonstrated that batches of zinc white exhibit stark binary or ternary X-ray absorption behavior at the Zn L-edge. Based on a fundamental investigation of the XANES absorption features and the symmetries of defects in the ZnO lattice, it was hypothesized that the dominant binary distinction between ZnO crystallites is related to differences in populations of low-symmetry intrinsic crystal defects. The chemically distinct third group of crystallites was identified as hydrozincite: the product of long-term exposure of ZnO to atmospheric CO_2 and water vapor. The observation of a binary distinction throughout all analyzed ZnO samples strongly suggests that the presence of two distinct fractions of ZnO

particles within a batch is inherently linked to the vapor oxidation synthesis method and its spatially variable synthesis parameters. The observation of hydrozincite and its nanometric spatial distribution suggests that some ZnO crystallites are more reactive toward CO_2 and water vapor than others and that this may be related to the binary distinction revealed in the X-ray absorption behavior.

Overall, the results presented in this article provide important new pieces of information to help us understand the link between the intrinsic properties of zinc white and its reactivity in oil paint. Moreover, the discussed link between intrinsic crystal defect populations and synthesis parameters may prove valuable for the applications of ZnO in catalysis, photonics, and electronics, where the defect population crucially affects performance.

■ ASSOCIATED CONTENT

Ⓢ Supporting Information

The Supporting Information is available free of charge at https://pubs.acs.org/doi/10.1021/acs.jpcc.0c03381.

　　Detailed information about processing and visualization of STXM energy stacks (PDF)

■ AUTHOR INFORMATION

Corresponding Author

Selwin Hageraats − *Rijksmuseum, Conservation and Science, 1070DN Amsterdam, The Netherlands; IPANEMA, CNRS, Ministère de la Culture et de la Communication, Université de Versailles Saint-Quentin-en-Yvelines, USR 3461, Université Paris-Saclay, 91128 Gif-sur-Yvette, France; Van't Hoff Institute for Molecular Science, University of Amsterdam, 1090GD Amsterdam, The Netherlands;* ⓞ orcid.org/0000-0002-1583-1371; Email: s.hageraats@rijksmuseum.nl

Authors

Katrien Keune − *Rijksmuseum, Conservation and Science, 1070DN Amsterdam, The Netherlands; Van't Hoff Institute for Molecular Science, University of Amsterdam, 1090GD Amsterdam, The Netherlands*

Slavica Stankic − *Sorbonne Université, CNRS, Institut des NanoSciences de Paris, INSP, F-75005 Paris, France;* ⓞ orcid.org/0000-0002-8711-9746

Stefan Stanescu − *Synchrotron SOLEIL, 91192 Cedex Gif-Sur-Yvette, France*

Moniek Tromp − *Materials Chemistry, Zernike Institute for Advanced Materials, 9747AG Groningen, The Netherlands;* ⓞ orcid.org/0000-0002-7653-1639

Mathieu Thoury − *IPANEMA, CNRS, Ministère de la Culture et de la Communication, Université de Versailles Saint-Quentin-en-Yvelines, USR 3461, Université Paris-Saclay, 91128 Gif-sur-Yvette, France*

Complete contact information is available at:
https://pubs.acs.org/10.1021/acs.jpcc.0c03381

Author Contributions

The manuscript was written through contributions of all authors. All authors have given approval to the final version of the manuscript.

Notes

The authors declare no competing financial interest.

■ REFERENCES

(1) Kühn, H. In *Artists' Pigments: A Handbook of Their History and Characteristics*; Feller, R. L., Ed.; Archetype Publications: London, 1986; Vol. *1*, pp 169−186.

(2) Jacobsen, A. E.; Gardner, W. H. Zinc Soaps in Paints: Zinc Oleates. *Ind. Eng. Chem.* **1941**, *33*, 1254−1256.

(3) Rogala, D.; Lake, S.; Maines, C.; Mecklenburg, M. Condition Problems Related to Zinc Oxide Underlayers: Examination of Selected Abstract Expressionist Paintings from the Collection of Hirshhorn Museum and Sculpture Garden, Smithsonian Institution. *J. Am. Inst. Conserv.* **2010**, *49*, 96−113.

(4) Helwig, K.; Poulin, J.; Corbeil, M.-C.; Moffat, E.; Duguay, D. In *Issues in Contemporary Oil Paint*; Van den Berg, K. J., Burnstock, A., Keijzer, M., Krueger, J., Learner, T., de Tagle, A., Heydenreich, G., Eds.; Springer: Cham, 2014; pp 167−184.

(5) Baij, L.; Hermans, J. J.; Keune, K.; Iedema, P. D. Time-Dependent ATR-FTIR Spectroscopic Studies on Fatty Acid Diffusion and the Formation of Metal Soaps in Oil Paint Model Systems. *Angew. Chem., Int. Ed.* **2018**, *57*, 7351−7354.

(6) Catalano, J.; Murphy, A.; Yao, Y.; Zumbulyadis, N.; Centeno, S. A.; Dybowski, C. In *Metal Soaps in Art*; Casadio, F., Keune, K., Noble, P., Van Loon, A., Hendriks, E., Centeno, S. A., Osmond, G., Eds.; Springer: Houten, 2019; pp 69−84.

(7) Rosi, F.; Cartechini, L.; Monico, L.; Gabrieli, F.; Vagnini, M.; Buti, D.; Doherty, B.; Anselmi, C.; Brunitti, B. G.; Miliani, C. In *Metal Soaps in Art*; Casadio, F., Keune, K., Noble, P., Van Loon, A., Hendriks, E., Centeno, S. A., Osmond, G., Eds.; Springer: Houten, 2019; pp 173−193.

(8) Hermans, J. J.; Baij, L.; Koenis, M.; Keune, K.; Iedema, P. D.; Woutersen, S. 2D-IR Spectroscopy for Oil Paint Conservation: Elucidating the Water-Sensitive Structure of Zinc Carboxylate Clusters in Ionomers. *S. Sci. Adv.* **2019**, *5*, No. eaaw3592.

(9) Hageraats, S.; Keune, K.; Réfrégiers, M.; Van Loon, A.; Berrie, B.; Thoury, M. Synchrotron Deep-UV Photoluminescence Imaging for the Submicrometer Analysis of Chemically Altered Zinc White Oil Paints. *Anal. Chem.* **2019**, *91*, 14887−14895.

(10) Osmond, G.; Ebert, B.; Drennan, J. Zinc Oxide-Centred Deterioration in 20th-Century Vietnamese Paintings by Nguyễn Trọng Kiệm (1933−1991). *AICCM Bulletin* **2014**, *34*, 4−14.

(11) Hageraats, S.; Keune, K.; Thoury, M.; Hoppe, R. In *Conservation of Modern Oil Paintings*; Van den Berg, K. J., Bonaduce, I., Burnstock, A., Ormsby, B., Scharff, M., Carlyle, L., Heydenreich, G., Keune, K., Eds.; Springer: Cham, 2019; pp 275−288.

(12) Osmond, G. In *Issues in contemporary oil paint*; Van den Berg, K. J., Burnstock, A., Keijzer, M., Krueger, J., Learner, T., de Tagle, A., Heydenreich, G., Eds.; Springer: Cham, 2014; pp 263−281.

(13) Gabrieli, F.; Rosi, F.; Vichi, A.; Cartechini, L.; Buemi, L. P.; Kazarian, S. G.; Miliani, C. Revealing the Nature and Distribution of Metal Carboxylates in Jackson Pollock's Alchemy 1947. by Micro-Attenuated Total Reflection FT-IR Spectroscopic Imaging. *Anal. Chem.* **2017**, *89*, 1283−1289.

(14) French, S. A.; Sokol, A. A.; Bromley, S. T.; Catlow, C. R. A.; Rogers, S. C.; King, F.; Sherwood, F. From CO$_2$ to Methanol by Hybrid QM/MM Embedding. *Angew. Chem.* **2001**, *113*, 4569−4572.

(15) Kurtz, M.; Strunk, J.; Hinrichsen, O.; Muhler, M.; Fink, K.; Meyer, B.; Wöll, C. Active Sites on Oxide Surfaces: ZnO-Catalyzed Synthesis of Methanol from CO and H$_2$. *Angew. Chem., Int. Ed.* **2005**, *44*, 2790−2794.

(16) Drouilly, C.; Krafft, J.-M.; Averseng, F.; Lauron-Pernot, H.; Bazer-Bachi, D.; Chizallet, C.; Lecocq, V.; Costentin, G. Origins of the Deactivation Process in the Conversion of Methylbutynol on Zinc Oxide Monitored by Operando DRIFTS. *Catal. Today* **2013**, *205*, 67−75.

(17) Pugnet, V.; Maury, S.; Coupard, V.; Dandeu, A.; Quoineaud, A.-A.; Bonneau, J.-L.; Tichit, D. Stability, Activity and Selectivity Study of a Zinc Aluminate Heterogeneous Catalyst for the Transesterification of Vegetable Oil in Batch Reactor. *Appl. Catal., A* **2010**, *374*, 71−78.

(18) Yan, S.; Salley, S. O.; Ng, K. Y. S. Simultaneous Trans-esterification and Esterification of Unrefined or Waste Oils over ZnO-La$_2$O$_3$ Catalysts. *Appl. Catal., A* **2009**, *353*, 203−212.

(19) Bertrand, L.; Réfrégiers, M.; Berrie, B.; Échard, J.-P.; Thoury, M. A Multiscalar Photoluminescence Approach to Discriminate Among Semiconducting Historical Zinc White Pigments. *Analyst* **2013**, *138*, 4463−4469.

(20) Özgür, Ü.; Alivov, Y. I.; Liu, C.; Teke, A.; Reshchikov, M. A.; Dogan, S.; Avrutin, V.; Cho, S.-J.; Morkoç, H. A Comprehensive Review of ZnO Materials and Devices. *J. Appl. Phys.* **2005**, *98*, 041301.

(21) Djurišić, A. B.; Chen, X.; Leung, Y. H.; Ng, A. M. C. ZnO Nanostructures: Growth, Properties and Applications. *J. Mater. Chem.* **2012**, *22*, 6526−6535.

(22) Djurišić, A. B.; Leung, Y. H.; Tam, K. H.; Hsu, Y. F.; Ding, L.; Ge, W. K.; Zhong, Y. C.; Wong, K. S.; Chan, W. K.; Tam, H. L.; et al. Defect Emissions in ZnO Nanostructures. *Nanotechnology* **2007**, *18*, 095702.

(23) Zhang, M.; Averseng, F.; Haque, F.; Borghetti, P.; Krafft, J.-M.; Baptiste, B.; Costentin, G.; Stankic, S. Defect-Related Multicolour Emissions in ZnO Smoke: from Violet, over Green to Yellow. *Nanoscale* **2019**, *11*, 5102−5115.

(24) Rösner, B.; Koch, F.; Döring, F.; Bosgra, J.; Guzenko, V. A.; Kirk, E.; Meyer, M.; Ornelas, J. L.; Fink, R. H.; Stanescu, S.; et al. Exploiting Atomic Layer Deposition for Fabricating Sub-10 nm X-Ray Lenses. *Microelectron. Eng.* **2018**, *191*, 91−96.

(25) Wang, Y. F.; Shao, Y. C.; Hsieh, S. H.; Chang, Y. K.; Yeh, P. H.; Hsueh, H. C.; Chiou, J. W.; Wang, H. T.; Ray, S. C.; Tsai, H. M.; et al. Origin of Magnetic Properties in Carbon Implanted ZnO Nanowires. *Sci. Rep.* **2018**, *8*, 7758.

(26) Chiou, J. W.; Jan, J. C.; Tsai, H. M.; Bao, C. W.; Pong, W. F.; Tsai, M.-H.; Hong, I.-H.; Klauser, R.; Lee, J. F.; Wu, J. J.; Liu, S. C. Electronic Structure of ZnO Nanorods Studied by Angle-Dependent X-Ray Absorption Spectroscopy and Scanning Photoelectron Microscopy. *Appl. Phys. Lett.* **2004**, *84*, 3462−3464.

(27) Yan, W.; Sun, Z.; Liu, Q.; Li, Z.; Pan, Z.; Wang, D.; Zhou, Y.; Zhang, X.; et al. Zn Vacancy Induced Room-Temperature Ferromagnetism in Mn-Doped ZnO. *Appl. Phys. Lett.* **2007**, *91*, 062113.

(28) Singh, S. B.; Wang, Y. F.; Shao, Y. C.; Lai, H. Y.; Hsieh, S. H.; Limaye, M. V.; Chuang, C. H.; Hsueh, H. C.; Wang, H.; Chiou, J. W.; et al. Observation of the Origin of d^0 Magnetism in ZnO Nanostructures Using X-Ray-Based Microscopic and Spectroscopic Techniques. *Nanoscale* **2014**, *6*, 9166−9176.

(29) Thurau, C.; Kersting, C. K.; Wahabzada, M.; Bauckhage, C. Descriptive Matrix Factorization for Sustainability: Adopting the Principle of Opposites. *Data Min. Knowl. Discovery* **2012**, *24*, 325−354.

(30) Pholnak, C.; Sirisathitkul, C.; Suwanboon, S.; Harding, D. J. Effects of Precursor Concentration and Reaction Time on Sonochemically Synthesized ZnO Nanoparticles. *Mater. Res.* **2014**, *17*, 405−411.

(31) Cho, D.-Y.; Kim, J. H.; Na, K. D.; Song, J.; Hwang, C. S.; Park, B.-G.; Kim, J.-Y.; Min, C.-H.; Oh, S.-J. Spectroscopic Evidence for Limited Carrier Hopping Interaction in Amorphous ZnO Thin Film. *Appl. Phys. Lett.* **2009**, *95*, 261903.

(32) Wasinger, E. C.; De Groot, F. M. F.; Hedman, B.; Hodgson, K. O.; Solomon, E. I. L-edge X-ray Absorption Spectroscopy of Non-Heme Iron Sites: Experimental Determination of Differential Orbital Covalency. *J. Am. Chem. Soc.* **2003**, *125*, 12894−12906.

(33) Patel, M.; Aswath, P. B. Morphology, Structure and Chemistry of Extracted Diesel Soot: Part II: X-ray Absorption Near Edge Structure (XANES) Spectroscopy and High Resolution Transmission Electron Microscopy. *Tribol. Int.* **2012**, *52*, 17−28.

(34) Ghose, S. The Crystal Structure of Hydrozincite, $Zn_5(OH)_6(CO_3)_2$. *Acta Crystallogr.* **1964**, *17*, 1051−1057.

(35) Meyer, B. K.; Sann, J.; Hofmann, D. M.; Neumann, C.; Zeuner, A. Shallow Donors and Acceptors in ZnO. *Semicond. Sci. Technol.* **2005**, *20*, S62−S66.

(36) Look, D. C.; Hemsky, J. W.; Sizelove, J. R. Residual Native Shallow Donor in ZnO. *Phys. Rev. Lett.* **1999**, *82*, 2552−2555.

(37) Vidya, R.; Ravindran, P.; Fjellvåg, H.; Svensson, B. G.; Monakhov, E.; Ganchenkova, M.; Nieminen, R. M. Energetics of Intrinsic Defects and Their Complexes in ZnO Investigated by Density Functional Calculations. *Phys. Rev. B: Condens. Matter Mater. Phys.* **2011**, *83*, 045206.

(38) Janotti, A.; Van de Walle, C. G. Oxygen Vacancies in ZnO. *Appl. Phys. Lett.* **2005**, *87*, 122102.

(39) Erhart, P.; Klein, A.; Albe, K. First-Principles Study of the Structure and Stability of Oxygen Defects in Zinc Oxide. *Phys. Rev. B: Condens. Matter Mater. Phys.* **2005**, *72*, 085213.

(40) Janotti, A.; Van de Walle, C. G. Fundamentals of Zinc Oxide as a Semiconductor. *Rep. Prog. Phys.* **2009**, *72*, 126501.

(41) Hausmann, A.; Schallenberger, B. Interstitial Oxygen in Zinc Oxide Single Crystals. *Z. Phys. B: Condens. Matter Quanta* **1978**, *31*, 269−273.

(42) Janotti, A.; Van de Walle, C. G. New Insights into the Role of Native Point Defects in ZnO. *J. Cryst. Growth* **2006**, *287*, 58−65.

(43) Kim, D.-H.; Lee, G.-W.; Kim, Y.-C. Interaction of zinc interstitial with oxygen vacancy in zinc oxide: An origin of n-type doping. *Solid State Commun.* **2012**, *152*, 1711−1714.

(44) Kim, Y.-S.; Park, C. H. Rich Variety of Defects in ZnO via an Attractive Interaction between O Vacancies and Zn Interstitials: Origin of *n*-Type Doping. *Phys. Rev. Lett.* **2009**, *102*, 086403.

(45) Van de Walle, C. G.; Neugebauer, J. First-Principles Calculations for Defects and Impurities: Applications to III-Nitrides. *J. Appl. Phys.* **2004**, *95*, 3851−3879.

(46) Artesani, A.; Gherardi, F.; Nevin, A.; Valentini, G.; Comelli, D. A Photoluminescence Study of the Changes Induced in the Zinc White Pigment by Formation of Zinc Complexes. *Materials* **2017**, *10*, 340.

(47) Levine, K. E.; Collins, B. J.; Stout, M. D.; Wyde, M.; Afton, S. E.; Essader, A. S.; Ennis, T. J.; Amato, K. E.; McWilliams, A. C.; Fletcher, B. L.; et al. Characterization of Zinc Carbonate Basic as a Source of Zinc in a Rodent Study Investigating the Effects of Dietary Deficiency or Excess. *Anal. Lett.* **2017**, *50*, 2447−2464.

(48) Ohkuma, N.; Funayama, Y.; Ito, H.; Mizutani, N.; Kato, M. Reaction of Carbon Dioxide Containing Water Vapor with ZnO Fine Particles. *Nippon Kagaku Kaishi* **1987**, *5*, 802−806.

(49) Stavale, F.; Nilius, N.; Freund, H.-J. STM Luminescence Spectroscopy of Intrinsic Defects in ZnO (0001) Thin Films. *J. Phys. Chem. Lett.* **2013**, *4*, 3972−3976.

(50) Xu, P. S.; Sun, Y. M.; Shi, C. S.; Xu, F. Q.; Pan, H. B. The Electronic Structure and Spectral Properties of ZnO and its defects. *Nucl. Instrum. Methods Phys. Res., Sect. B* **2003**, *199*, 286−290.